Chapter 5

SAXS Evaluation of Size Distribution for Nanoparticles

Shinichi Sakurai

Additional information is available at the end of the chapter

http://dx.doi.org/10.5772/105981

Abstract

Size distribution is an important structural aspect in order to rationalize relationship between structure and property of materials utilizing polydisperse nanoparticles. One may come to mind the use of dynamic light scattering (DLS) for the characterization of the size distribution of particles. However, only solution samples can be analyzed and even for those, the solution should be transparent or translucent because of using visible light. It is needless to say that solid samples are out of range. Furthermore, the size distribution only in the range of several tens of nanometers can be characterized, so DLS is useless for particles in the range of several nanometers. Therefore, the small-angle X-ray scattering (SAXS) technique is much superior when considering the determination of the size distribution in several nanometers length scale for opaque solutions and for solid specimens. Furthermore, the SAXS technique is applicable not only for the spherical particle but also for platelet (lamellar) and rod-like (cylindrical) particles. In this chapter, we focus on the form factor of a variety of nanostructures (spheres, prolates, core-shell spheres, core-shell cylinders and lamellae). Also getting started with a monodisperse distribution of the size of the nanostructure, to unimodal distribution with a narrow standard deviation or wide-spreading distribution and finally to the discrete distribution can be evaluated by the computational parameter fitting to the experimentally obtained SAXS profile. In particular, for systems forming complicated aggregations, this methodology is useful. Not only the size distribution of 'a bunch of grapes' but also the size distribution of all 'grains of grapes in the bunch' can be evaluated according to this methodology. This is very much contrasted to the case of the DLS technique by which only 'a bunch of grapes' is analyzed but 'grains of grapes in the bunch' cannot be. It is because the DLS technique in principle evaluates diffusion constants of particles and all of the grains in the same bunch of grapes diffuse as a whole. Thus, the methodology is important to highlight versatility and diversity in real materials, especially in soft matter, both in the liquid and in the solid states.

Keywords: SAXS, form factor, sphere, cylinder, lamella, prolate, core-shell sphere, core-shell cylinder, discrete distribution function

1. Introduction

In recent years, controlling of nanostructures has been more significantly considered in the field of materials science, especially relating to the soft matter [1]. Versatile properties or functions can be obtained through designing nanostructures in solid-state materials, as well as nanomaterials dispersed in liquid-state substance. Even for contradictory properties such as hard and soft, they may be coexistent in one material when fabricating so-called inclined nanostructures (for instance, nanoparticle size is gradually changing as a function of the position in material). This in turn indicates that size distribution of the nanostructures should be rigorously evaluated for better understanding effects of nanostructure on properties and functions. For biological systems or supramolecular organizations, situation is very much contrast to the other ubiquitous materials as described above because they form spontaneously a regular aggregation. Therefore, the size distribution is narrow and follows a simple mathematical function with a comparatively small standard deviation. By contrast, discrete distribution of the size is required to determine for the ubiquitous materials. However, even for regular nanostructures, the determination of the discrete distribution of the nanostructure size is needed to reveal a transient state upon transition from the state 1 to the state 2, being triggered by sudden change in temperature, pH, or other external parameters.

It is well known that the size distribution of particles can be evaluated by the use of dynamic light scattering (DLS). However, only solution samples can be analyzed and even for those, the solution should be transparent or translucent because of using visible light. It is needless to say that solid samples are out of range. Furthermore, the size distribution only in the range of several tens of nanometers can be characterized, so DLS is useless for particles in the range of several nanometers. Therefore, the small-angle X-ray scattering (SAXS) technique is much superior when considering the determination of the size distribution in several nanometers length scale for opaque solutions and for solid specimens [2]. Furthermore, the SAXS technique is applicable, not only for the spherical particle but also for platelet (lamellar) and rod-like (cylindrical) particles and it enables us to determine the thickness distribution of lamellae or the cross-sectional radius distribution of cylinders. Namely, the SAXS technique does not matter types of particle shape even for hallow cylinders or hollow spheres [3].

The principle is simple. Scattering comprises not only contribution from regularity of space-filling ordering (the lattice factor) of particles but also from a single particle (the form factor). The particle scattering can be mathematically formulated depending on the type of particle shape (lamella, cylinder or sphere). In the block copolymer microdomain systems, the Gauss distribution of the particle size has been assumed. Only recently, direct determination of the discrete size distribution has been available by conducting fitting theoretical scattering function to the experimentally obtained SAXS profile (the plot of the scattering intensity as a function of the magnitude of the scattering vector, q [= $(4\pi/\lambda)$ sin $(\Theta/2)$ with Θ and λ being the scattering angle and the wavelength of X-ray, respectively] where the abundance of the particle having a given size was treated as a floating parameter with a step of 1 nm (the step can be more precise). In this chapter, getting started

with nanoparticles with a narrow size distribution, we will see characteristic shape of the form factors for protein self-assembly, block copolymer microdomains and peptide amphiphile nanofibers. Then, we shift our target to the evaluation of discrete distribution of size of nanostructures by SAXS. The examples shown are thickness distribution of the crystalline lamellae of polyethylene glycol in polymer blends and thickness distribution of the hard segment domains for supramolecular elastomers (starblocks of soft polyisobutylene and hard oligo(β-alanine) segments). Other notable examples are sterically stabilized polypyrrole-palladium (PPy-Pd) nanocomposite particles, hybrid amphiphilic poly(N-isopropylacrylamide)/metal cyanide complexes and the cobalt(II) terpyridine complexes with diblock copolypeptide amphiphiles. For this example, this methodology is useful. Not only the size distribution of 'a bunch of grapes' but also the size distribution of all 'grains of grapes in the bunch' can be evaluated according to this methodology. This is very much contrasted to the case of the DLS technique by which only 'a bunch of grapes' is analyzed but 'grains of grapes in the bunch' cannot be. It is because the DLS technique in principle evaluates diffusion constants of particles and all of the grains in the same bunch of grapes diffuse as a whole. Thus, the methodology is important to highlight versatility and diversity in real materials, especially in soft matter, both in the liquid and in the solid states.

2. Nanoparticles with a narrow size distribution

First of all, some typical examples of the experimentally observed form factor are demonstrated. The samples are self-assembly of proteins, block copolymer microdomains and peptide amphiphiles. Apoferritin is a protein having ability to store iron atoms and it is referred to as ferritin when iron atoms are bound. Apoferritin forms a spherical shell as a self-assembled nanostructure with a very uniform size. As indicated in **Figure 1** (pH-dependence of SAXS profiles), its SAXS profiles (apoferritin, 24-mer) exhibit characteristic features with many peaks due to its uniform shape for pH ≥3.40 [4]. Dramatic change in the SAXS profile is detected between pH = 1.90 and 3.40. This means that apoferritin is disassembled for acidic condition. Time-resolved SAXS measurements have been utilized to study disassembling and reassembling process upon the change in pH [4, 5]. In **Figure 1**, the curve shows the result of the SAXS modeling by the scattering program GNOM [6]. Since protein molecules produce the typical form factor, it is frequently used to obtain commissioning data for newly launched SAXS beamline or apparatus [7–9].

It is known that block copolymer spontaneously forms a regular nanostructure with a narrow size distribution. **Figure 2** shows examples of the SAXS profiles for sphere-forming block copolymer (SEBS; polystyrene-block-poly(ethylene-co-butylene)-block-polystyrene triblock copolymer) having Mn = 6.7×10^4, Mw/Mn = 1.04, PS volume fraction = 0.084) [10], where Mn and Mw denote number-average and weight-average molecular weights, respectively. In **Figure 2**, the solid curve is the results of the model calculation for the spherical particle, but not only the form factor, but also the lattice factor of BCC (body-centered cubic) is taken into account. The full equation is as follows [11–14]:

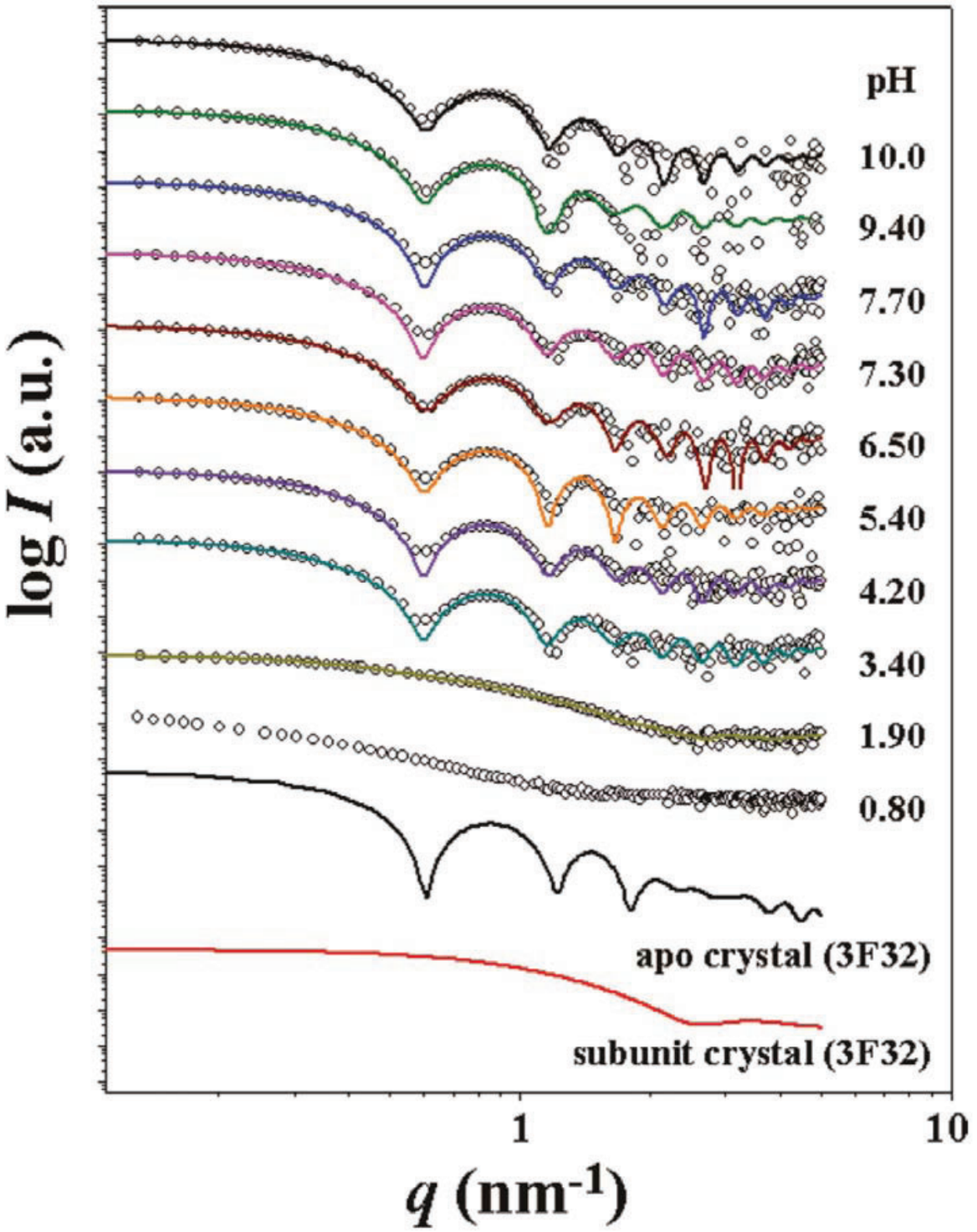

Figure 1. pH-dependence of SAXS profiles for an apoferritin aqueous solution. The symbols indicate the experimental data, and the solid lines indicate the fits obtained using the GNOM program. The solid lines without symbols are the theoretical SAXS curves calculated from the crystal structure of apoferritin and its subunit crystal (PDB code 3F32). For clarity, each plot is shifted along the log I axis [4].

http://dx.doi.org/10.5772/105981

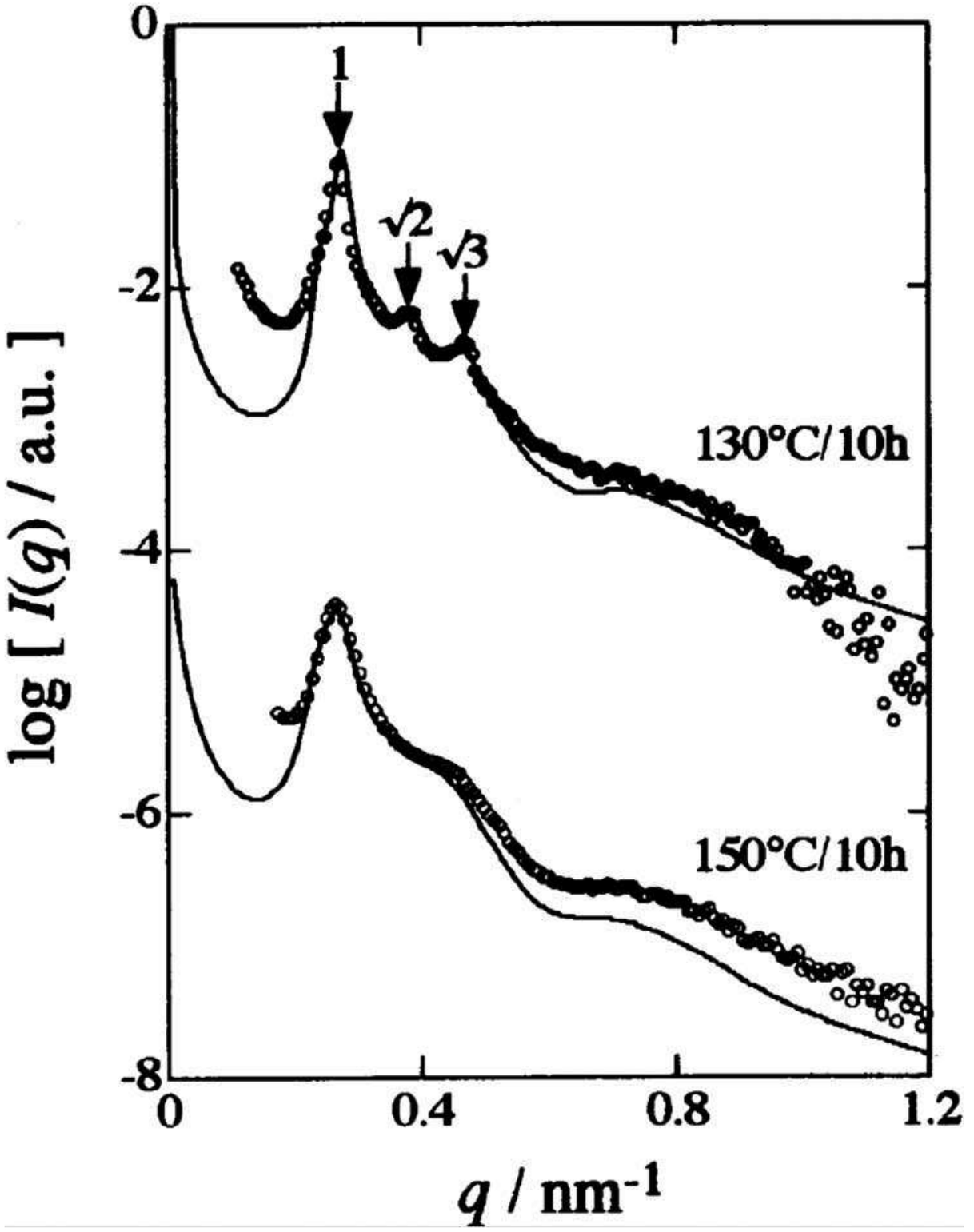

Figure 2. SAXS profiles for SEBS-8 specimens (sphere-forming triblock copolymer) annealed at 130 and 150°C for 10 h [10].

$$I(q) - \langle |f^2(q)| \rangle - |\langle f(q) \rangle|^2 + |\langle f(q) \rangle|^2 Z(q) \tag{1}$$

where <x> is the average of the quantity of x. $f(q)$ and $Z(q)$ are particle and lattice factor, respectively, designating the scattering amplitude due to the intraparticle interference and the scattering intensity due to the interparticle interference, respectively. The form factor $f(q)$ for a spherical particle with its radius, R, can be given as

$$f(q) = A_e \Delta\rho \, V \frac{3[\sin(qR) - qR\cos(qR)]}{(qR)^3} \tag{2}$$

where A_e is the scattering amplitude of the Thomson scattering, $\Delta\rho$ is the difference in the electron density between sphere and matrix, V is the volume of the spheres. Here, the Gauss distribution is used for R with σ_R being the standard deviation. On the other hand, the lattice factor $Z(q)$ is given by Eq. (3) with Eulerian angles, θ and ϕ, which define orientation of the unit cell of a given grain with respect to the experimental Cartesian coordinates:

$$\begin{aligned} Z(q,\theta,\phi) = & \frac{1 - F_k^2}{\left[1 - 2F_k \cos\left(\frac{\sqrt{6}}{4} qd\alpha\right) + F_k^2\right]} \\ & \times \frac{1 - F_k^2}{\left[1 - 2F_k \cos\left(\frac{\sqrt{6}}{4} qd\beta\right) + F_k^2\right]} \times \frac{1 - F_k^2}{\left[1 - 2F_k \cos\left(\frac{\sqrt{6}}{4} qd\gamma\right) + F_k^2\right]} \end{aligned} \tag{3}$$

with

$$F_k = \exp\left[-\frac{3}{16} g^2 d^2 q^2 (\alpha^2 + \beta^2 + \gamma^2)\right] \tag{4}$$

and $g = \Delta d / \langle d \rangle$ which is the degree of the lattice distortion (Δd denotes the standard deviation in d due to the paracrystalline distortion). In Eq. (4),

$$\alpha = \sin\theta\cos\phi + \sin\theta\sin\phi + \cos\theta \tag{5}$$

$$\beta = -\sin\theta\cos\phi - \sin\theta\sin\phi + \cos\theta \tag{6}$$

$$\gamma = -\sin\theta\cos\phi + \sin\theta\sin\phi - \cos\theta \tag{7}$$

for the bcc lattice and

$$\alpha = \sin\theta\sin\phi + \cos\theta \tag{8}$$

$$\beta = -\sin\theta\cos\phi + \cos\theta \tag{9}$$

$$\gamma = -\sin\theta\cos\phi + \sin\theta\sin\phi \tag{10}$$

for the fcc lattice. In Eqs. (3) and (4), d denotes the Bragg spacing. The spacing for {110} and {111} planes for the bcc and fcc lattices, respectively, gives rise to the first-order peaks. For

randomly oriented polygrains in actual samples, the scattering is isotropic. Therefore, $Z(q,\theta,\phi)$ is averaged with respect to θ and ϕ to obtain isotropic $Z(q)$:

$$Z(q) = \frac{1}{4\pi}\int_0^{2\pi}\int_0^{\pi} Z(q,\theta,\phi)\sin\theta d\theta d\phi \tag{11}$$

As clearly observed in **Figure 2**, the broad peak around q = 0.71 nm^{-1} is due to the form factor. The model curve is the result of calculation with <*R*> = 7.90 nm for 130°C annealed specimen and <*R*> = 8.10 nm for 150°C annealed specimen and the standard deviation of the size distribution (σ_R) being 1.09 and 1.10 nm, respectively. Thus, evaluated value of <*R*> is consistent with the result of transmission electron microscopic observation (as shown in **Figure 3**). Note also here that the order-disorder transition temperature locates between 130 and 150°C, so that bcc ordering is quite regular for the specimen annealed at 130°C, while it is poor for 150°C annealed specimen. The SAXS profile for the 130°C annealed specimen displays clear lattice peaks at the relative q values of 1:√2:√3, indicating high regularity of the bcc ordering. The sphere-forming block copolymers exhibit mostly the bcc ordering due to the entropic profit [14] and the fcc ordering has been found for some particular case. Comparison between the results shown in **Figures 1** and **2** clearly indicates that many peaks for monodisperse particle are easy to collapse to become more featureless when the size distribution is incorporated even if it is small. Nevertheless, it is characteristic for the block copolymer microdomains that one peak can be discernible for the form factor.

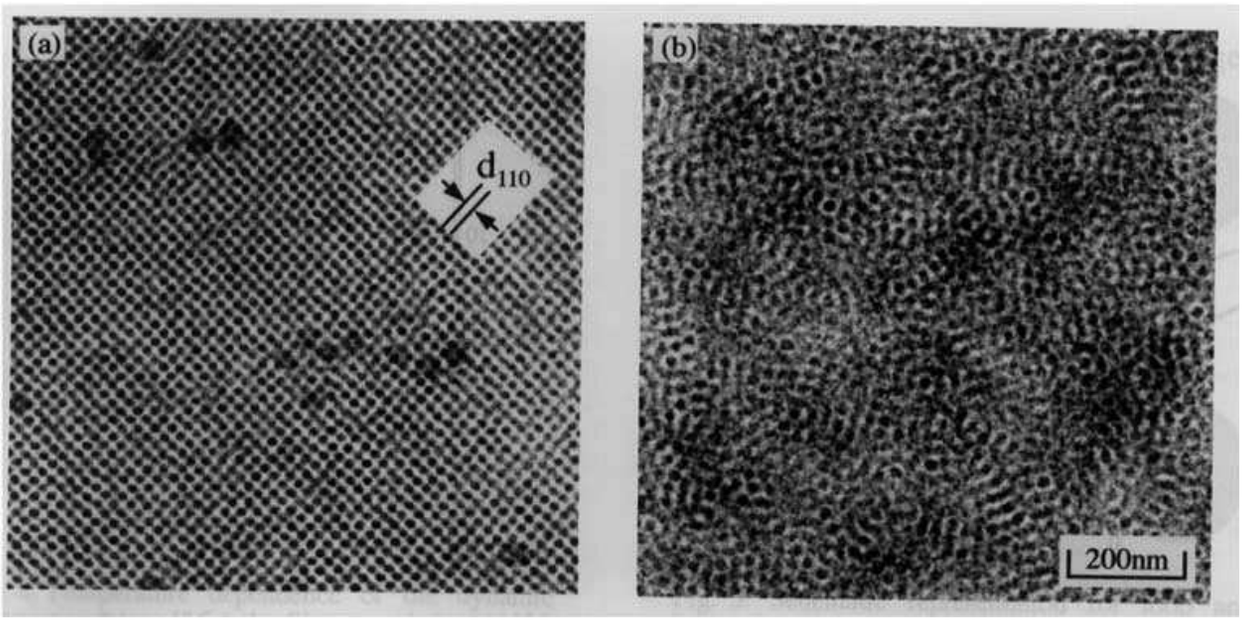

Figure 3. TEM micrographs for SEBS-8 specimens annealed at (a) 130 and (b) 150°C for 10 h. The polystyrene microdomains were stained with ruthenium tetroxide [10].

Very recently, it has been found that PS spherical microdomains were deformed upon the uniaxial stretching of the SEBS-8 film specimens [15]. Since SEBS triblock copolymer with the glassy PS spherical microdomains can be used as a thermoplastic elastomer (TPE), the film

specimen can be stretched. In **Figure 4**, 2D-SAXS patterns are displayed to recognize the deformation of the round shape form factor upon the uniaxial stretching. **Figure 4a** shows the 2D-SAXS pattern for the SEBS-8 film specimen. Here, it is clearly observed that the round shape form factor appears at q = 0.77 nm^{-1}. The round peak of the form factor is deformed to become an ellipsoid in **Figure 4b** upon uniaxial stretching of the film specimen up to the strain of 3.65 (stretching ratio is 4.65) at room temperature. The peak position in the $\boldsymbol{q}^{-}$direction parallel to the stretching direction ($\boldsymbol{q}$//SD) is lower than that in the $\boldsymbol{q}^{-}$direction perpendicular to SD ($\boldsymbol{q}\perp$SD). This means that the size of the particle in the $\boldsymbol{q}_{//}$ direction is bigger than that in $\boldsymbol{q}_{\perp}$ direction, which in turn implies deformation of the spherical particles. Therefore, the model calculation of the form factor, $P(q)$, for prolate was conducted using the mathematical equation as follows:

$$P(q) = \int_0^{2\pi} \int_0^{\pi/2} \int_0^{\infty} \int_1^{\infty} f^2(q, v, R_{\min}, \phi)\ \Omega(v)\ \Xi(R_{\min})\ \Psi_{\phi}(\phi)\Psi_{\mu}(\mu) \sin\phi\ dv\ dR_{\min}\ d\phi d\mu \tag{12}$$

$$f(q, v, R_{\min}) = V\frac{3(\sin U - U\cos U)}{U^3} \tag{13}$$

$$U(q, v, R_{\min}, \phi) = qR_{\min}\sqrt{\sin^2\phi + v^2\cos^2\phi} \quad for\ q//SD \tag{14}$$

$$U(q, v, R_{\min}, \phi, \mu) = qR_{\min}\sqrt{\sqrt{1-\sin^2\phi\cos^2\mu} + v^2\sin^2\phi\cos^2\mu} \quad \text{for } q\perp\text{SD} \tag{15}$$

$$v = \frac{R_{\text{maj}}}{R_{\min}} > 1 \qquad V = \frac{4\pi}{3}R_{maj}R_{\min}^2 = \frac{4\pi}{3}vR_{\min}^3 \quad \text{and (volume of the prolate)} \tag{16}$$

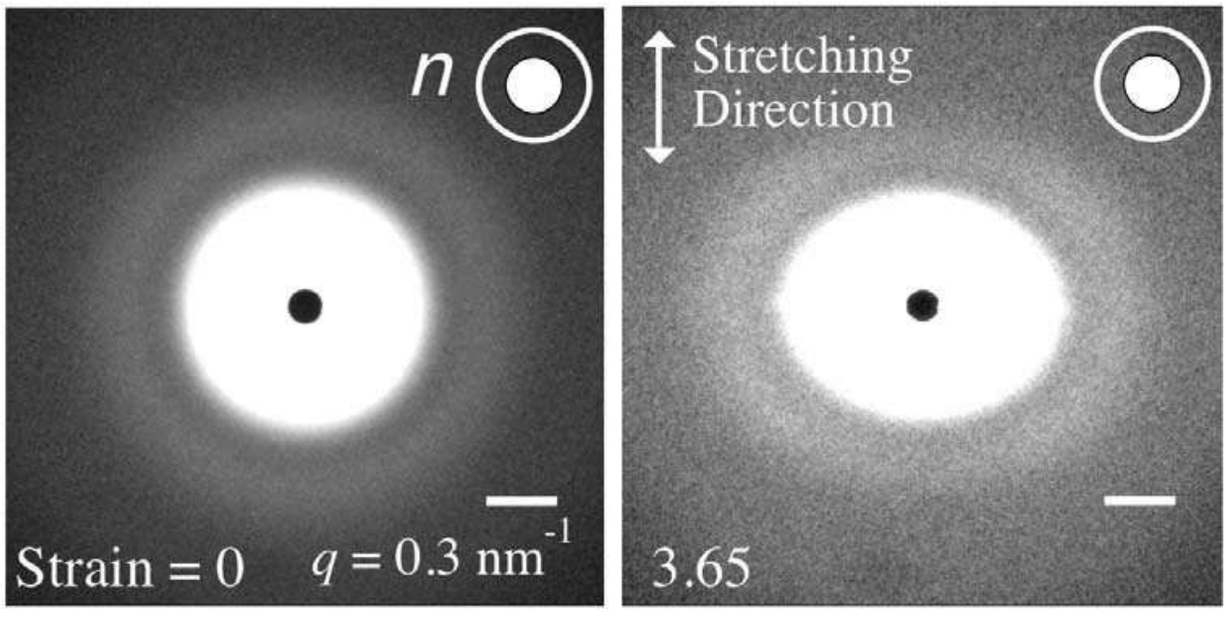

Figure 4. 2D-SAXS patterns for SEBS-8 specimens (a) unstretched state and (b) being stretched at the strain of 3.65 at room temperature [15].

Here, R_{maj} and R_{min} stand for the radius of the longer axis and the radius of the shorter axis of the prolate, respectively (**Figure 5**) and ϕ is the angle between the $\boldsymbol{q}$ direction and the long axis of the prolate. To fit the SAXS profile with the model calculation, the distributions in R_{min}, ν and ϕ are required. Note here that the distributions in ϕ and μ define the orientational distribution function: $\Psi_{\phi}(\phi)$ and $\Psi_{\mu}(\mu)$, respectively. However, for this particular case, ϕ can be considered to be zero with no distribution, namely perfect orientation of the prolates with their log axes parallel to SD because the uniaxial stretching prolongs spherical microdomains to result in prolates with their long axes parallel to SD, which in turn enables us to set $\Psi_{\mu}(\mu) = 1$ regardless of μ. Therefore, due to decreased numbers of the parameters, the situation became easier to evaluate the average values of R_{min} and ν with their distributions (ΞR_{min} and $\Omega(\nu)$).

The results for the 1D-SAXS profiles in $\boldsymbol{q}_{//}$ and in $\boldsymbol{q}_{\perp}$ directions are shown in **Figure 6a** and **b**, respectively. In the both cases, the 1D-SAXS profile for the unstretched film specimen (before the stretching) is shown together. It is clearly observed that the peak of the form factor moved toward lower and higher q range upon the stretching in $\boldsymbol{q}_{//}$ and in $\boldsymbol{q}_{\perp}$ directions, respectively. Furthermore, both of the SAXS profiles can be fit by the prolate model, using Eqs. (1), (12)–(16) with the bcc lattice factor. Here, the $<R_{min}>$ = 6.44 nm and $<\nu>$ = 1.20 were used for the model calculation. Note that $<R_{min}>$ = 6.85 nm for the unstretched specimen. Moreover, the distributions in R_{min} and ν (ΞR_{min} and $\Omega(\nu)$) used for the calculation are plotted in **Figure 7a** and **b**, respectively. Such a mathematical function for the size distribution is enough to explain the experimentally observed SAXS profile under the stretched state. However, it should be noted that both of the distributions were required and otherwise, the model SAXS curve did not fit well the experimental results for both the $\boldsymbol{q}_{//}$ and $\boldsymbol{q}_{\perp}$ directions. **Figure 6a** and **b** also includes the SAXS profiles measured after complete removal of the stretching force. At a first glance, the peak positions of the form factor in **Figure 6a** and **b** seem to recover its original position for the unstretched specimens. However, this does not imply the recovery of the original spherical shape upon the removal of the load because the deformation of the glassy PS microdomains is permanent. Then, why did the form factor recover its original peak position? It may be ascribed to randomization of the prolates orientation upon the removal of the load. To check this speculation, we conducted the SAXS modeling of the prolate form factor by setting $\Psi(\phi) = 1$ irrespective of ϕ but with keeping the size distribution R_{min} and ν (ΞR_{min} and $\Omega(\nu)$) unchanged. The results of the modeling are shown with the red curves in **Figure 6a** and **b**, indicating clearly good agreements with the experimentally obtained SAXS profiles. This in turn confirms the speculation of randomization of the prolates orientation upon the removal of the load.

Core-shell sphere and cylinder models are significantly important for the amphiphilic self-assembly. For the core-shell sphere [16, 17], the form factor is formulated as:

$$P(q) = \left\{ (\rho_C - \rho_S) V_C \frac{3[\sin(qR_C) - qR_C \cos(qR_C)]}{(qR_C)^3} + (\rho_S - \rho_0) V_S \frac{3[\sin(qR_S) - qR_S \cos(qR_S)]}{(qR_S)^3} \right\}^2 \quad (17)$$

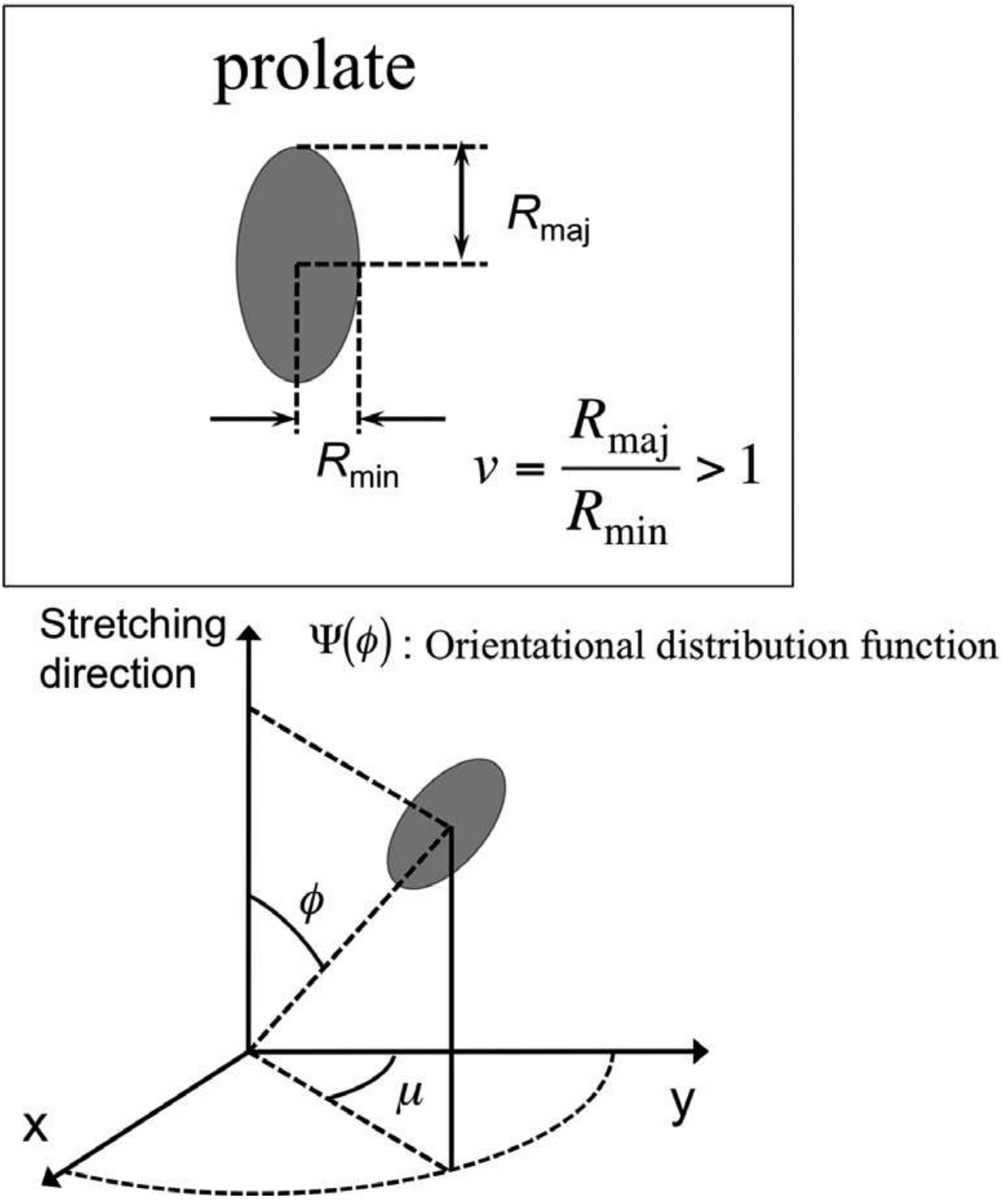

Figure 5. Prolate model used for the SAXS modeling. Here, R_{maj} and R_{min} stand for the radius of the longer axis and the radius of the shorter axes of the prolate, respectively. Eulerian angles, μ and ϕ, define orientation of the prolate with respect to the experimental Cartesian coordinates [15].

http://dx.doi.org/10.5772/105981

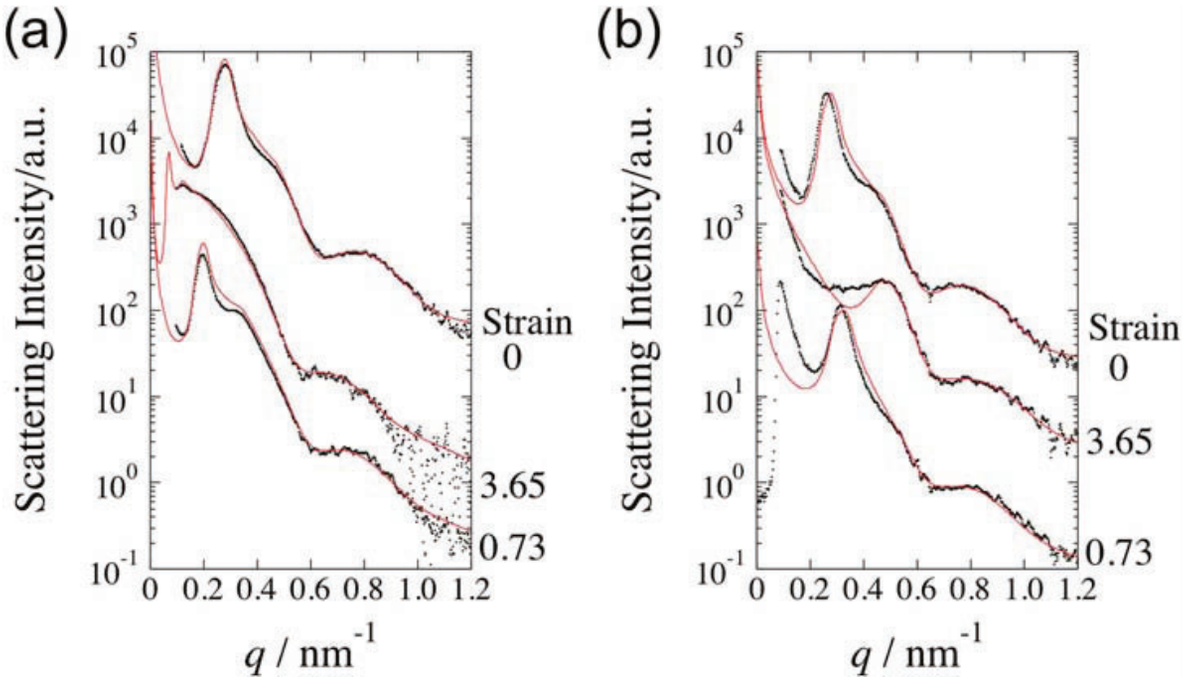

Figure 6. 1D-SAXS profiles extracted from the SAXS patterns as shown in **Figure 5** in (a) $q_{//}$ and in (b) $q_{\perp}$ directions. Black dots are for the experimentally obtained SAXS profiles, and red curves are calculated SAXS profiles [15].

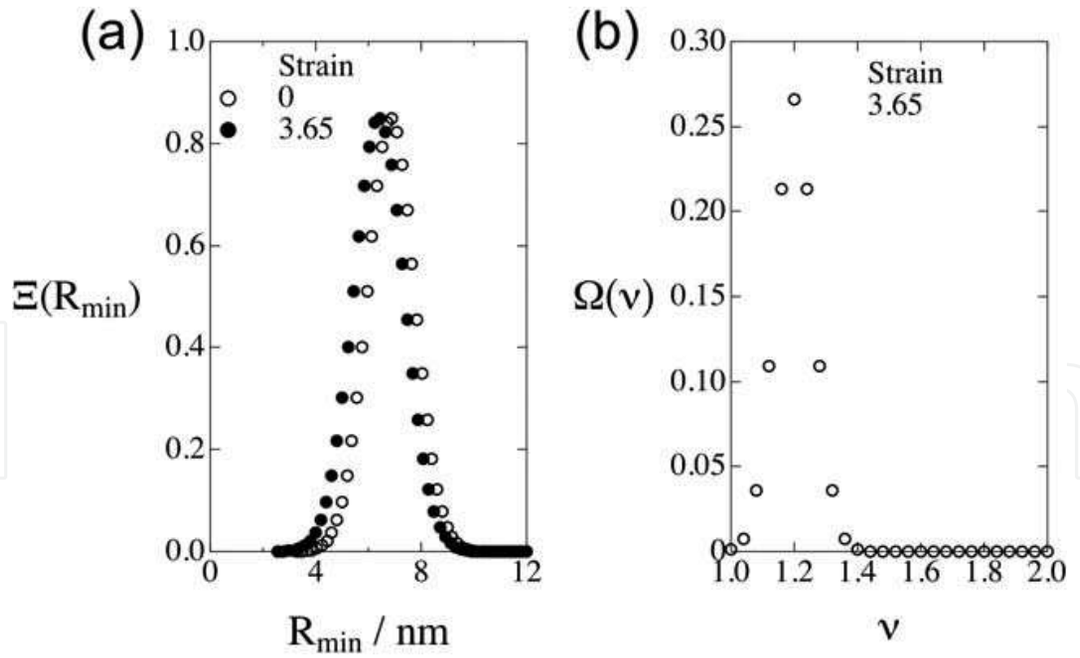

Figure 7. Evaluated $\Xi(R_{\min})$ and $\Omega(\nu)$ of the prolate for SEBS-8 specimens stretched at the strain of 3.65. For comparison, the size distribution function for the radius of sphere is shown together for the unstretched specimen [15].

if the homogeneous densities in the core and in the shell can be assumed with ρ_c and ρ_s, respectively. Here, V_c and V_s designate the volume of the core and the shell, respectively. Moreover, R_c and R_s denote the radii of the core and the shell, respectively. ρ_0 is the electron density of the matrix. On the other hand, when the shell density changes as a function of r (the core density is homogeneous) as defined with $\rho_s(r)$, then the form factor is formulated as [18, 19]:

$$P(q) = \left\{ (\rho_C - \rho_S) V_C \frac{3[\sin(qR_C) - qR_C \cos(qR_C)]}{(qR_C)^3} + 4\pi \int_{R_C}^{R_S} \left(\rho_S(r) - \rho_0\right) r^2 \frac{\sin(qr)}{qr} dr \right\}^2 \quad (18)$$

As for core-shell cylinders, the form factor is:

$$P(q) = \int_0^{\pi/2} \left\{ (\rho_S - \rho_{solv}) V_S \frac{\left[\sin\left(\frac{qH_S \cos\theta}{2}\right)\right]}{\frac{qH_S \cos\theta}{2}} \frac{2J_1(qR_S \sin\theta)}{qR_S \sin\theta} + \right.$$
$$\left. (\rho_C - \rho_S) V_C \frac{\left[\sin\left(\frac{qH_C \cos\theta}{2}\right)\right]}{\frac{qH_C \cos\theta}{2}} \frac{2J_1(qR_C \sin\theta)}{qR_C \sin\theta} \right\}^2 \sin\theta d\theta \quad (19)$$

where $J_1(x)$ is the first-order Bessel function. θ is defined as the angle between the cylinder axis and $\boldsymbol{q}$. R_C and R_S are the core and shell radii, respectively. H_C and H_S are the core and shell lengths, respectively. V_C and V_S are the core and shell volumes, respectively ($V_x = \pi R_x^2 H_x$; x = C, S, or $solv$; C: core, S: shell, $solv$: solvent). ρ_x is the electron density of the core, shell, or solvent.

Matson et al. [20] have reported the SAXS modeling of the form factor of the core-shell cylinder for self-assembling peptide amphiphiles (PAs) as shown in **Figure 8A** and **B**. The molecules self-assembled into the core-shell cylinder are illustrated in **Figure 8C**. Such cylinders can be detected with cryogenic TEM as shown in **Figure 9**. The SAXS profile is shown in **Figure 10** with the model curve, where the size distribution in the core radius is modeled using a log-normal distribution with the polydispersity being around 27–30% (see **Table 1** for the structural parameter determined by the SAXS modeling), while the radial shell thickness is assumed to be monodisperse. Although the modeling results explain very well the experimentally obtained SAXS profiles, the fact that the radial shell thickness is assumed to be monodisperse means it is difficult to determine individually two distributions in inner and outer radius. For more detailed structure analyses, more experimental variations are required to gather information from different kinds of aspects, like the example shown in **Figure 6a** and **b** (parallel and perpendicular to SD).

http://dx.doi.org/10.5772/105981

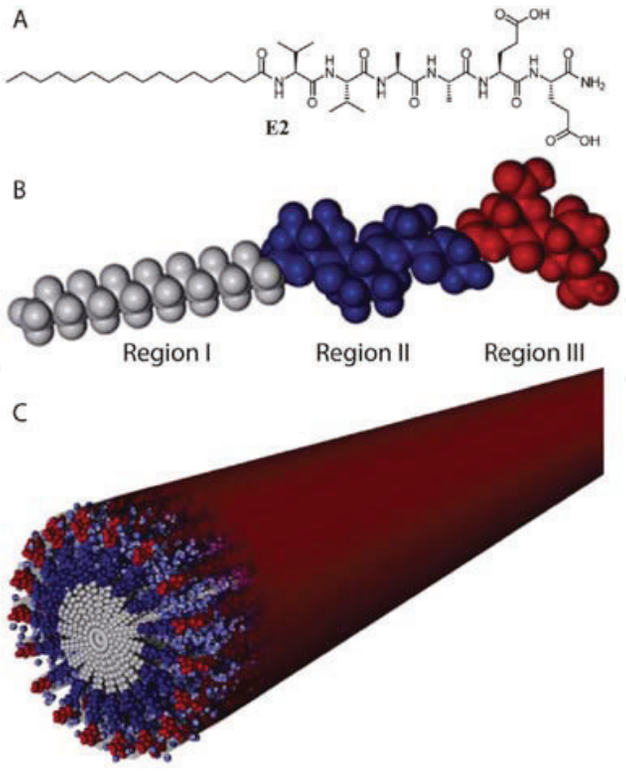

Figure 8. (A) Chemical structure of self-assembling peptide amphiphiles (PA: E2 C16V2A2E2). (B) The different regions of the PA are highlighted in a space-filling model. (C) Schematic illustration of a self-assembled PA nanofiber [20].

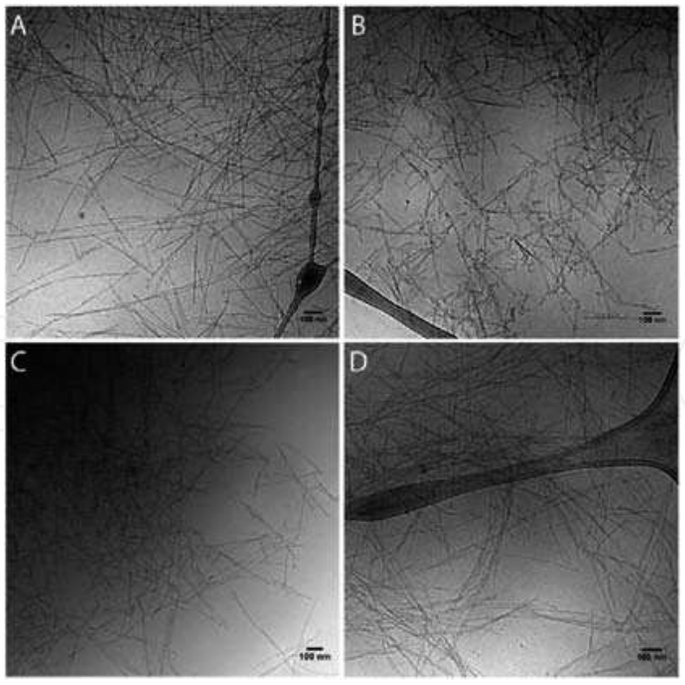

Figure 9. Cryogenic TEM of (A) PA 5, (B) PA 6, (C) PA 7, and (D) PA 8 as 1: 3 w/w mixtures with E2 PA [20].

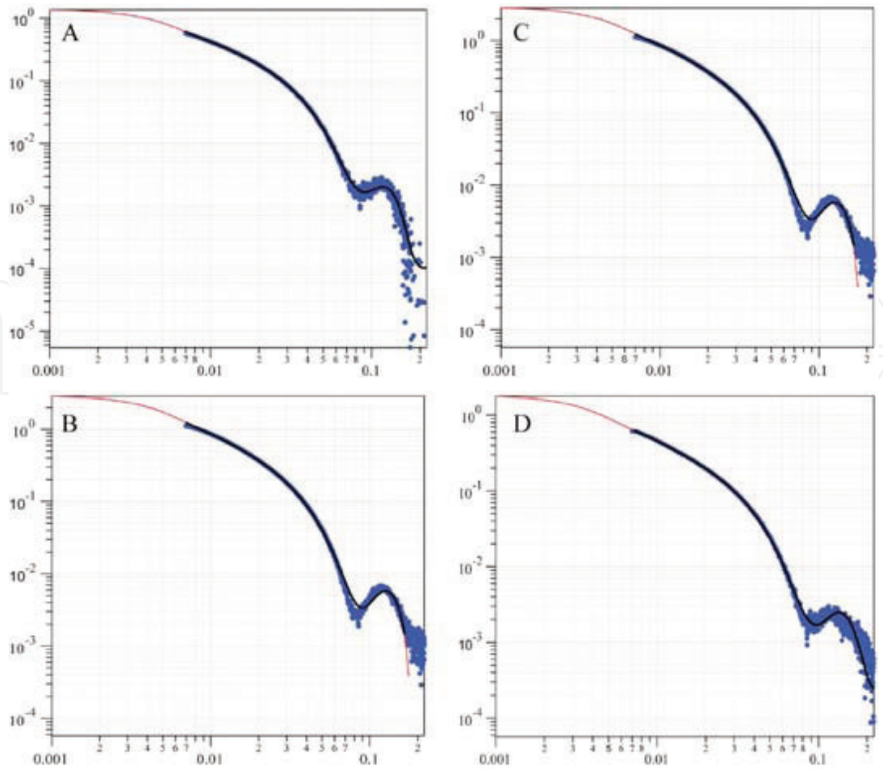

Figure 10. I SAXS profiles of PAs 5-8 (A-D) fitted to a polydisperse core-shell cylinder model. The solid red line represents the best fit to a core-shell cylinder form factor, where the core was allowed to be polydisperse according to a log-normal distribution. The solid black line represents the portion of the curves where fits were performed [20].

PA	5	6	7	8
Mean core radius (A)	12	12	12	12
Radial shell thickness (A)	29	27	25	25
Total diameter (nm)	8.2	7.8	7.4	7.4
Radial polydispersity (σ)	0.3	2.7	0.3	0.28

NaOH without $CaCl_2$ (from Ref. [20]).

Table 1. Selected SAXS data from PAs 5–8 at 0.25% in 4 mM.

3. Concept of evaluation of discrete distribution by SAXS

In this section, the concept of evaluation of the discrete distribution of the size of the nanostructure is explained. As an example, the lamellar model calculations are displayed in **Figure 11**, for which the mathematical equation is [21]:

$$P(q) = q^{-2}L^2[\{\sin(qL/2)\}/(qL/2)]^2 \tag{20}$$

where L is the lamellar thickness and the prefactor (q^{-2}) is the so-called Lorentz factor which is required to randomize the orientation of the lamellar particle. Here, it was assumed that the lamellar particle has infinitely large extent in the direction parallel to the lamellar surface.

Figure 11a and **b** shows the calculated profiles when L was set to 10 and 20 nm, respectively. It can be seen that the characteristics in the shapes of lamellar form factor are similar to the case of spherical form factor. As a matter of fact, many peaks appear. Summing up these two profiles gives the one, which is also shown in **Figure 11c**. This in turn means that the form factor is as shown in **Figure 11c** when the lamellar thickness distribution is as shown in the inset of **Figure 11**. It is noteworthy that the characteristic shape of the one shown in **Figure 11c** (L = 10 nm + L = 20 nm) is similar to the case of **Figure 11a** (L = 10 nm). When the distribution is somewhat modified as indicated in **Figure 12b**, the form factor is dramatically altered to the one as shown in **Figure 12a**. This seems to be no more characteristic form factor. Thus, the experimentally observed form factor can be a fingerprint and the size distribution may be evaluated as far as the shape of the nanostructure can be uniquely assumed.

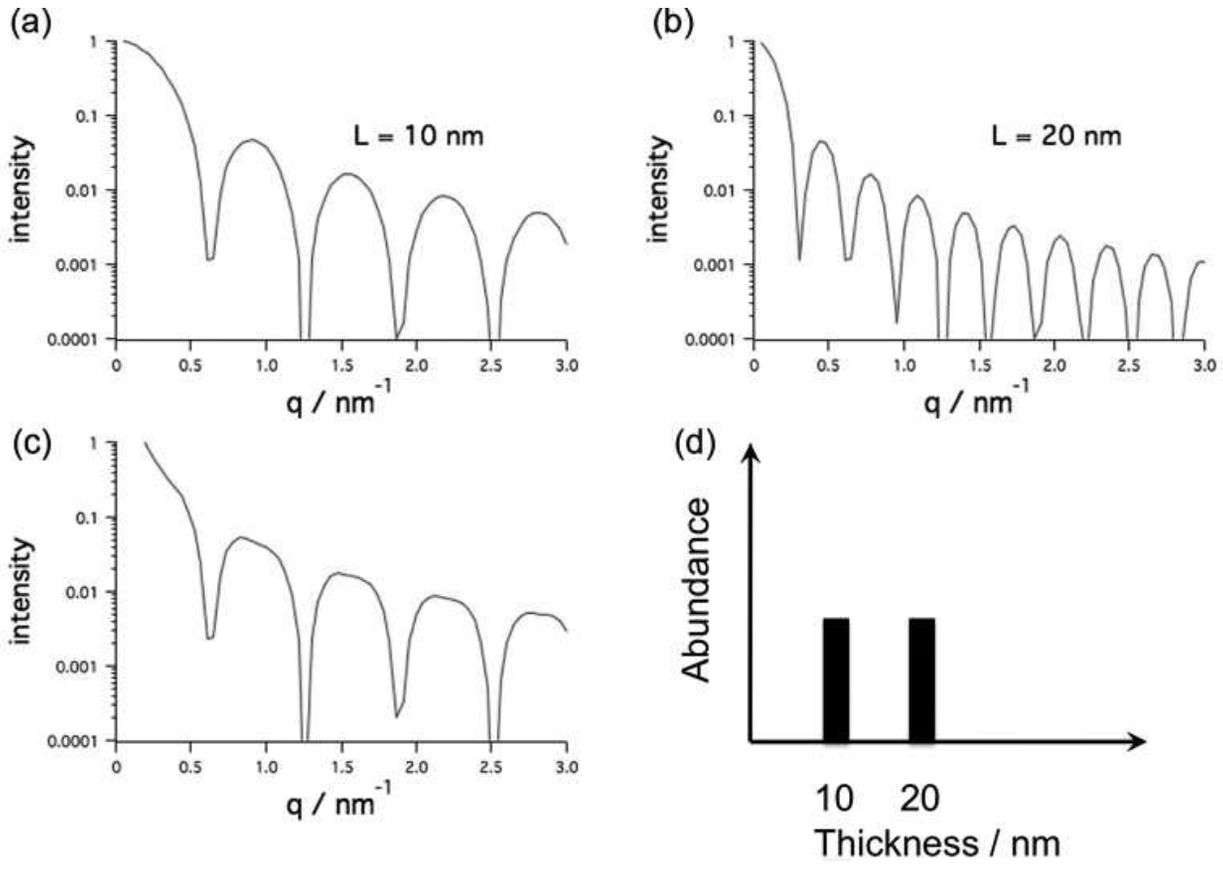

Figure 11. Calculated SAXS profiles for lamellar particle with (a) L = 10 nm, (b) L = 20 nm, and (c) L = 10 nm + L = 20 nm. The inset shows a hypothetical distribution function used for the calculation of the profile shown in **Figure 11c**.

Figure 12c shows one of the typical results of the SAXS profiles for poly(oxyethylene) (PEG), which forms lamellar crystallites. The exact sample used for the result of **Figure 12c** was a polymer blend of PEG with poly (D, L-lactide) (PDLLA), which is a racemic copolymer and therefore amorphous. The compositions of PEG/PDLLA were 80/20 (DL20) by weight. **Figure 12c** shows the result of the SAXS measurement at 64.0°C in the heating process [22].

At the temperature of 64.0°C slightly below the melting temperature of PEG (64.5°C), the typical form factor of lamellar particle was observed first time for the crystalline polymer. It was expected that the thinner lamellar which has a lower melting temperature melted away in the heating process. The thickest lamellae can only survive at the highest temperature and therefore, the thickness distribution became sharp. This may be the reason of the observation of the typical form factor of lamellar particle. As a matter of fact, a very sharp distribution was evaluated as shown in **Figure 12d** by the method described below.

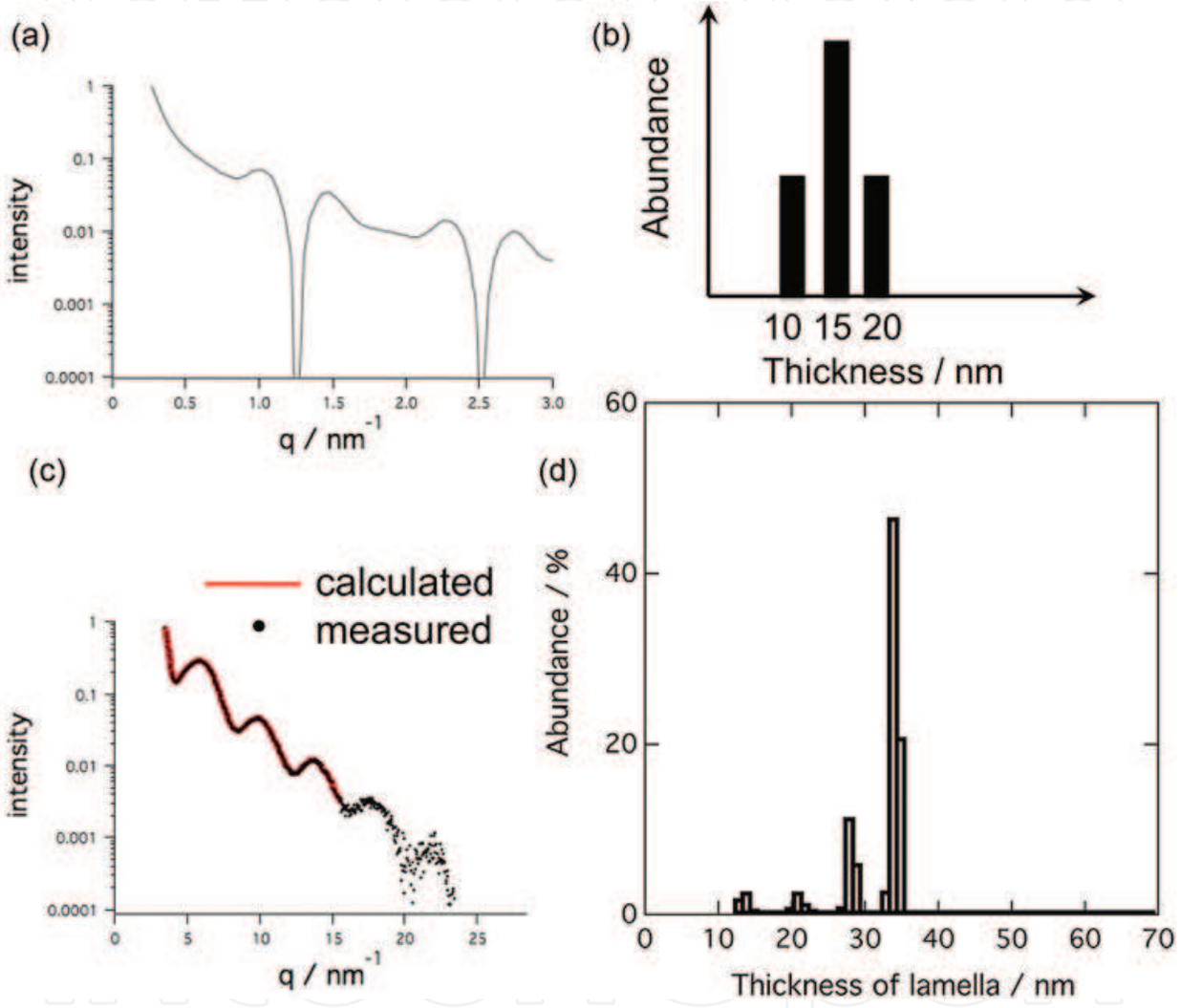

Figure 12. (a) Calculated SAXS profile for lamellar particle with assuming a hypothetical distribution function as shown in part (b). (c) One of the typical results of the SAXS profiles for PEG/PDLLA 80/20 blend at 64.0°C in the heating process. Black dots are for the experimentally obtained SAXS profile, and red curves are the calculated SAXS profile. (d) Evaluated thickness distribution from the result shown in part (c).

Hereafter, the data analysis method for the direct determination of the thickness distribution of lamellar particle is described. The model particle scattering intensity, $I(q)$, with a distribution of thicknesses can be given as:

$$I(\mathrm{q}) = k\Sigma[n(L)P(q)] \tag{21}$$

with $P(q)$ defined by Eq. (20). In Eq. (21), k is a numerical constant and $n(L)$ is the number fraction of lamella with a thickness of L, providing the thickness distribution of lamellae. A protocol was employed to directly determine $n(L)$ by fitting the calculated $I(q)$ from Eq. (21) to the experimentally observed 1D-SAXS profile where the following parameters were being floated as the fitting parameters: the numerical constant k and $n(L = 1$ nm), $n(L = 2$ nm), $n(L = 3$ nm),…, $n(L = 40$ nm) which are the abundance number of particles having thickness L in a step of 1 nm. By this protocol, the best fit was successfully performed, which is shown by the solid curve on the 1D-SAXS profile in **Figure 12c**. Although most of the features seem to be well described by the particle scattering, the first-order peak is not. For some SAXS profiles, the full calculation including the lattice factor $Z(q)$ and the particle scattering can describe the SAXS profile well. The mathematical formulation of $Z(q)$ is [23]:

$$Z(q) = \frac{1-|F|^2}{1-2|F|\cos(qD)+|F|^2} \tag{22}$$

$$|F| = \exp\left(-\frac{g^2D^2q^2}{2}\right) \tag{23}$$

Thus, the thickness distribution as shown in **Figure 12d** was also evaluated. Although such a sharp distribution around $L = 33.5$ nm accounts for the particle scattering dominant SAXS profile, the presence of thinner lamellae is clearly suggested.

4. Widely spread discrete distribution evaluated by SAXS

4.1. Lamellar case

Tien et al. have reported results of comprehensive studies of the higher-order crystalline structure of PEG in blends with PDLLA [22, 24, 25]. For several blend compositions, they have discussed the effects of blending PDLLA on the structural formation of PEG. It is remarkable that they found more regular higher-order structure for PEG 20 wt % composition (DL20) as compared to the PEG 100% sample in the as-cast blend sample (cast from a dichloromethane solution). More interestingly, they reported that the 1D-SAXS profile markedly changed from lattice peak dominant type to particle scattering dominant type when heating the as-cast sample, as shown in **Figure 13**. The compositions of PEG/PDLLA were 100/0, 95/5 (DL5), 90/10 (DL10) and 80/20 (DL20) by weight. **Figure 13** shows the results of the SAXS measurements in the heating process. Based on the results, we have conducted the evaluation of the lamellar thickness distribution in the heating process from the as-cast state up to 64°C and succeeded in showing that the distribution became sharper with the average thickness becoming larger, as shown in **Figure 14**. That study is the first showing quantitative evidence of the well-known concept of 'lamellar thickening' when a crystalline polymer is thermally annealed just below its melting temperature. Tien et al. have also conducted the same evaluation under higher pressure (5 and 50 MPa) [26].

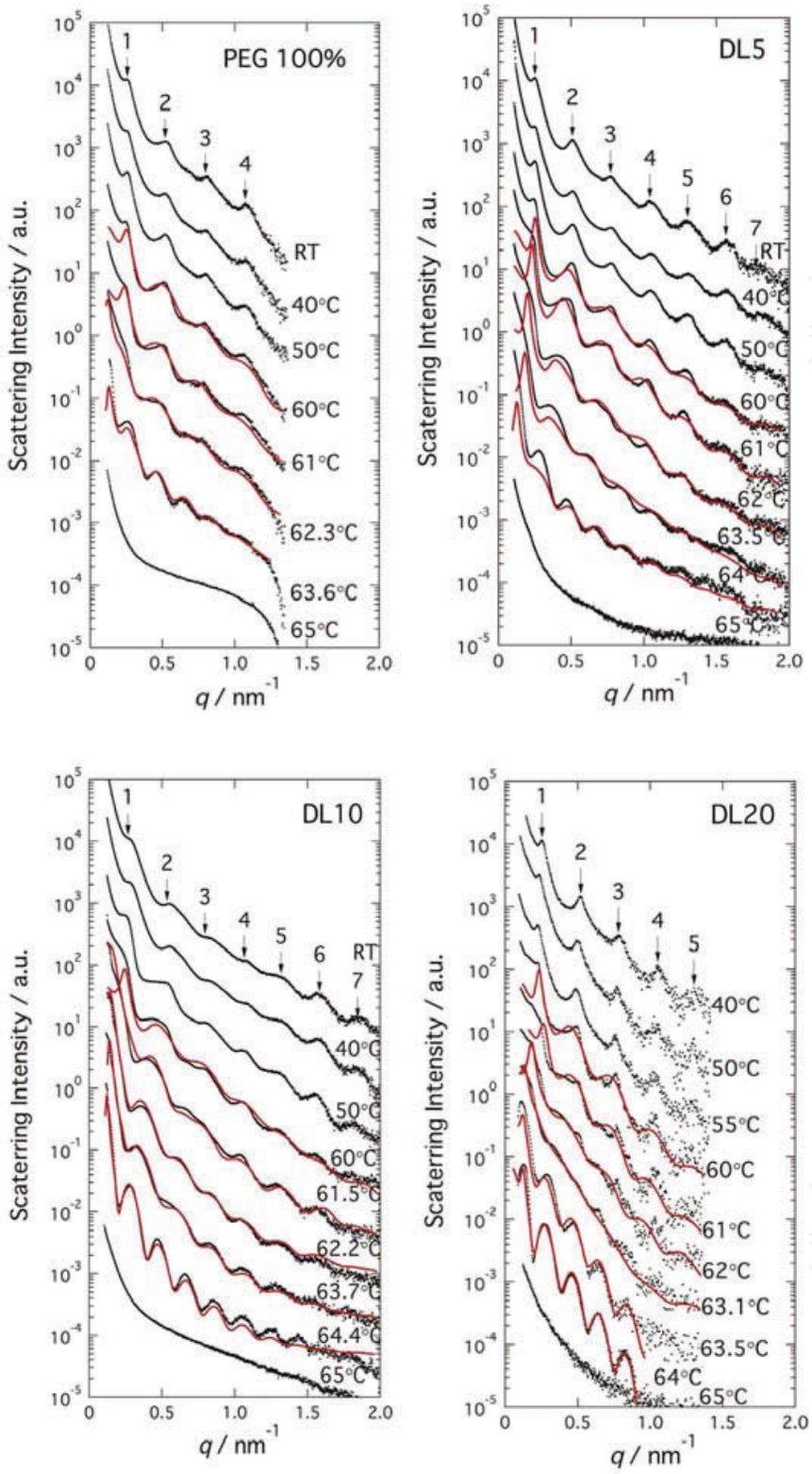

Figure 13. SAXS profiles for PEG/PDLLA blends with 100/0, 95/5 (DL5), 90/10 (DL10), and 80/20 (DL20) by weight. The SAXS measurements were conducted in the heating process. Black dots are for the experimentally obtained SAXS profiles, and red curves are the calculated SAXS profiles [22].

http://dx.doi.org/10.5772/105981

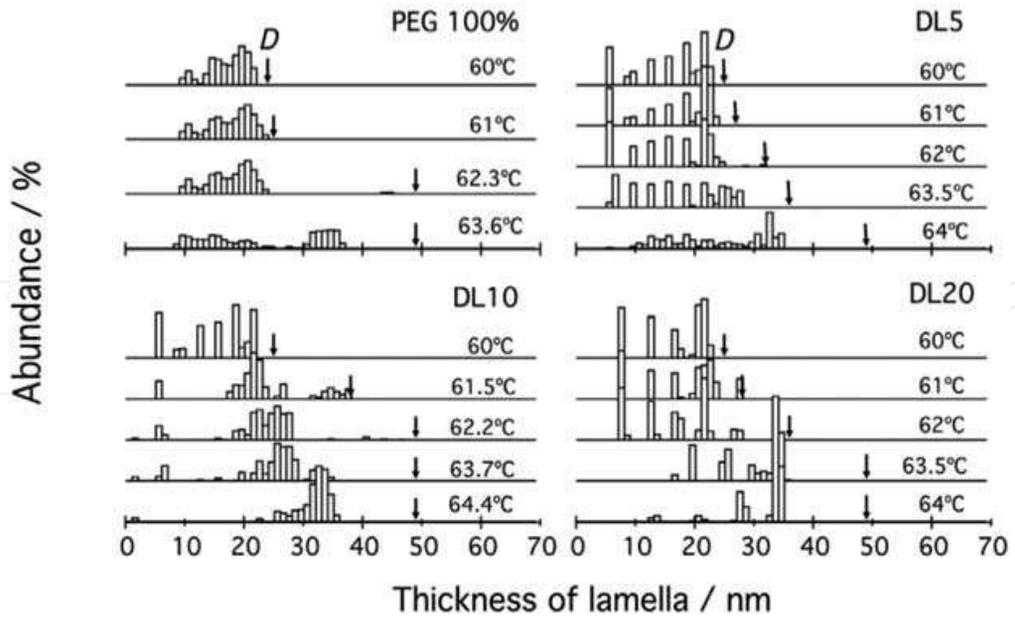

Figure 14. Evaluated thickness distribution from the result shown in **Figure 13** [22].

Jia et al. [27] have recently evaluated thickness distribution of the hard segment domains for supramolecular elastomers (starblocks of soft polyisobutylene and hard oligo(β-alanine) segments). The molecule is a novel type of supramolecule as schematically shown in **Figure 15** where the green chains are soft polyisobutylene. Due to the formation of the lamellar crystallites of oligo (β-alanine) segments, the specimen has rubber-like elasticity, that is, supramolecular self-assembly leads the specimen to TPE. Since such lamellar crystallites can be hardly observed by TEM, the SAXS measurement was conducted. The result is shown in **Figure 16** with the evaluated thickness distribution which is shown in the inset. Almost monodispersed distribution was evaluated with the peak at L = 2.0 nm (inset of **Figure 16**), which is in good agreement with the size of the oligo (β-alanine) contour length. This case clearly demonstrates the significance of the SAXS technique.

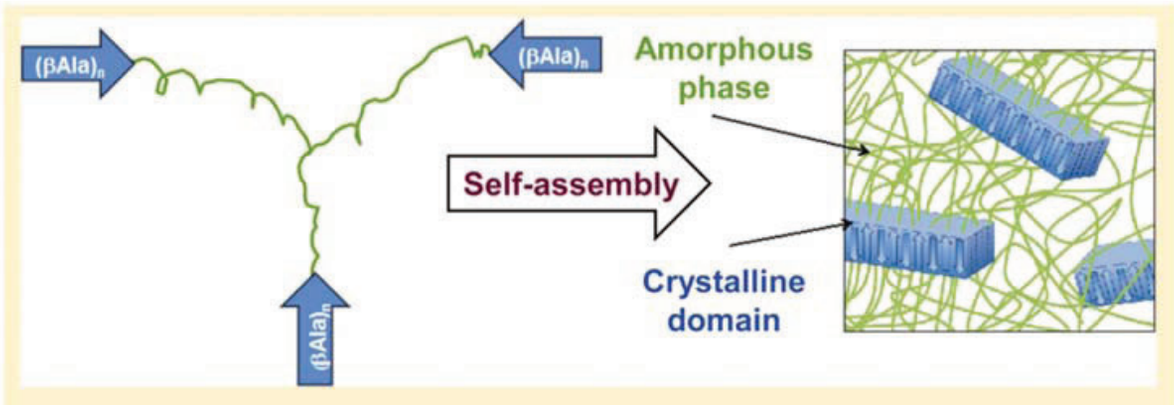

Figure 15. Schematic illustrations for supramolecular elastomers (starblocks of soft polyisobutylene and hard oligo(β-alanine) segments) where the green chains are soft polyisobutylene [27].

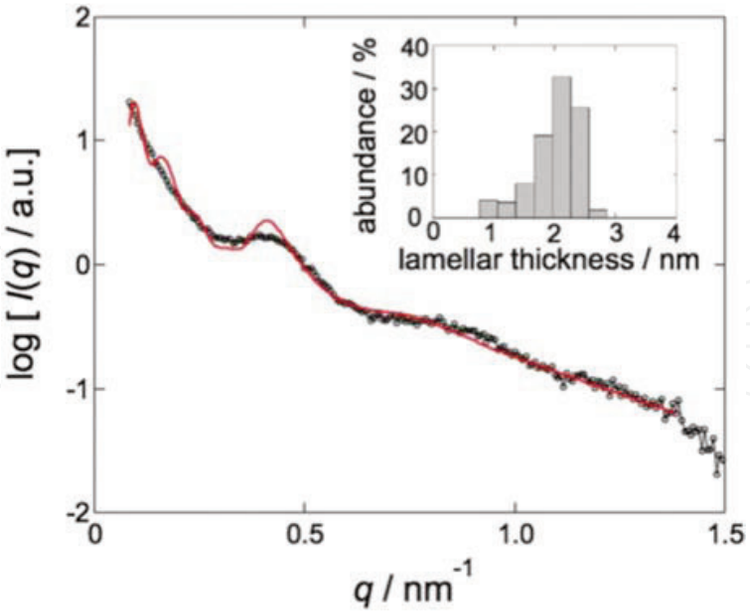

Figure 16. SAXS profile for the supramolecular elastomer schematically shown in **Figure 15**. Black dots are for the experimentally obtained SAXS profile, and red curve is the calculated SAXS profile. The inset shows the evaluated thickness distribution [27].

4.2. Spherical case

In this subsection, the size distribution of nanoparticles is described. Fujii et al. [28, 29] have synthesized novel for sterically stabilized polypyrrole-palladium (PPy-Pd) nanocomposite particles. Such a characteristic particle containing heavy element has recently been attracting intensively general interests of researchers in many fields under the name of element-blocks [30]. **Figure 17** shows a TEM image of these particles with a schematic of the structure. The ordinary 1D-SAXS profiles of 1, 2 and 3% aqueous dispersions of the nanocomposite particles are shown together in **Figure 18a** as a plot of log[$I(q)$] versus log q. This plot clearly shows that the shapes of the profiles are similar. When the curves are vertically shifted, all of the data collapse onto a single curve (**Figure 18b**), suggesting that the nanocomposite particles are dispersed in the aqueous medium without ordering into a lattice, at least up to a particle concentration of 3%. Thus, the 1D-SAXS profile can be attributed directly to the particle scattering (the form factor). Although the TEM results revealed that the nanocomposite particles are not spherical, a mathematical equation describing particle scattering is not available for such an unusual shape of particles. Therefore, a spherical shape is assumed for simplicity. The model particle scattering intensity, $I(q)$, with a distribution of thicknesses can be given as:

$$I(q) = k\Sigma[n(R)P(q)] \tag{24}$$

The form factor, $P(q)$, for spherical particles is given as:

$$P(q) = (4\pi R^3/3)^2[\Phi(q)]^2 \tag{25}$$

and

$$\Phi(q) = 3/(qR)^3[\sin(qR) - qR\cos(qR)] \tag{26}$$

http://dx.doi.org/10.5772/105981

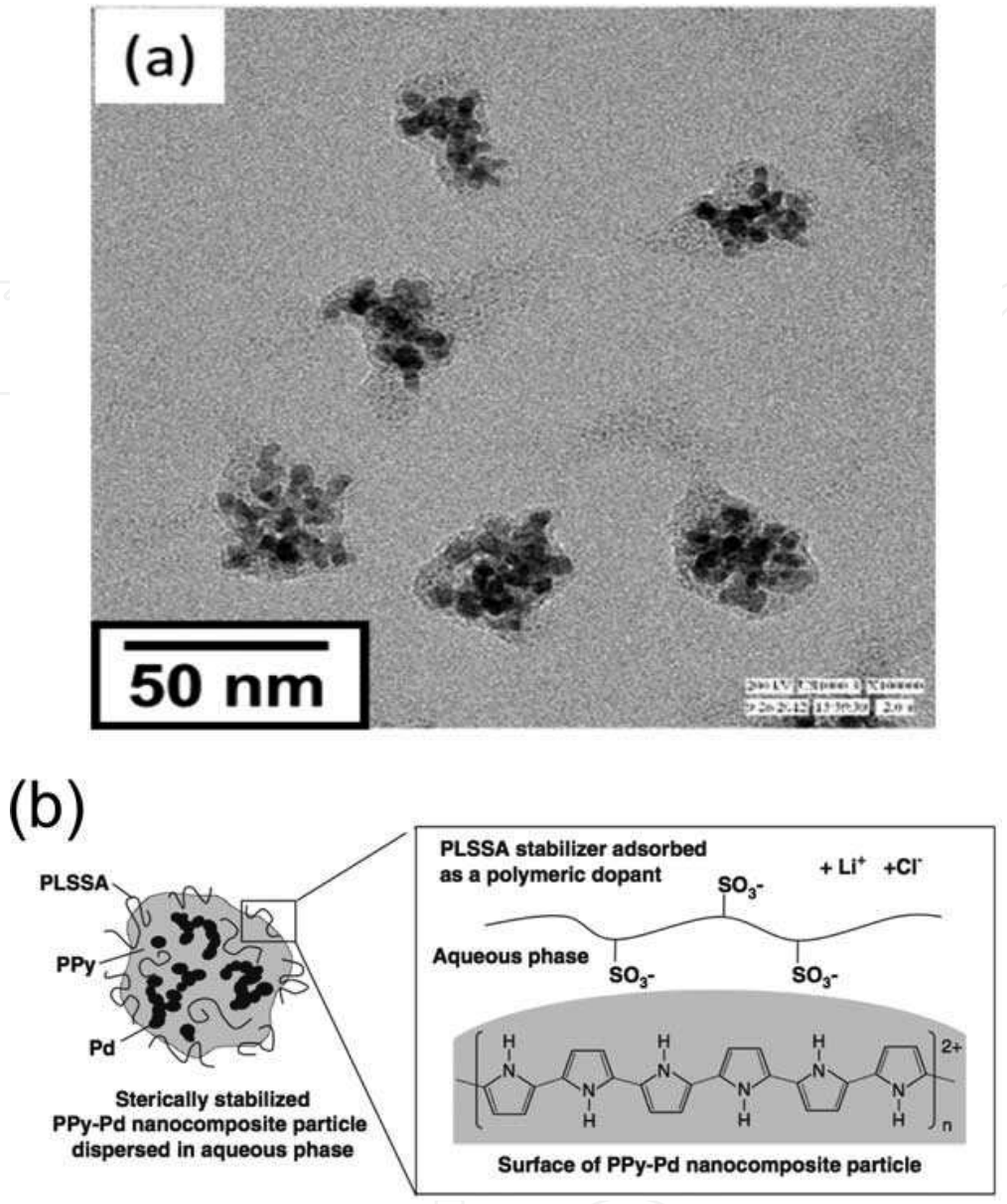

Figure 17. (a) TEM image of sterically stabilized polypyrrole-palladium (PPy-Pd) nanocomposite particles, and (b) a schematic of the structure [28].

In Eq. (24), k is a numerical constant and $n(R)$ is the number fraction of spheres with a radius of R, providing the size distribution of spheres. Attempts to fit a theoretical function given by Eq. (24) to the measured 1D-SAXS profile assuming a Gauss or Schulz-Zimm-type distribution for $n(R)$ were unsuccessful. We then employed a protocol in which $n(R)$ was directly determined by fitting the calculated $I(q)$ from Eq. (24) to the experimentally observed 1D-SAXS profile by the same method as described above for the lamellar case. The best fit is shown in **Figure 18a** with the dotted black curve for the 1D-SAXS profile (3% aqueous solution). The reason of using this profile is because of being most intense and therefore the most reliable. Thus, the obtained particle size distribution is shown in **Figure 19**, where the abundance is shown in the units of vol%, which was calculated by the following equation from the number fraction $n(R)$:

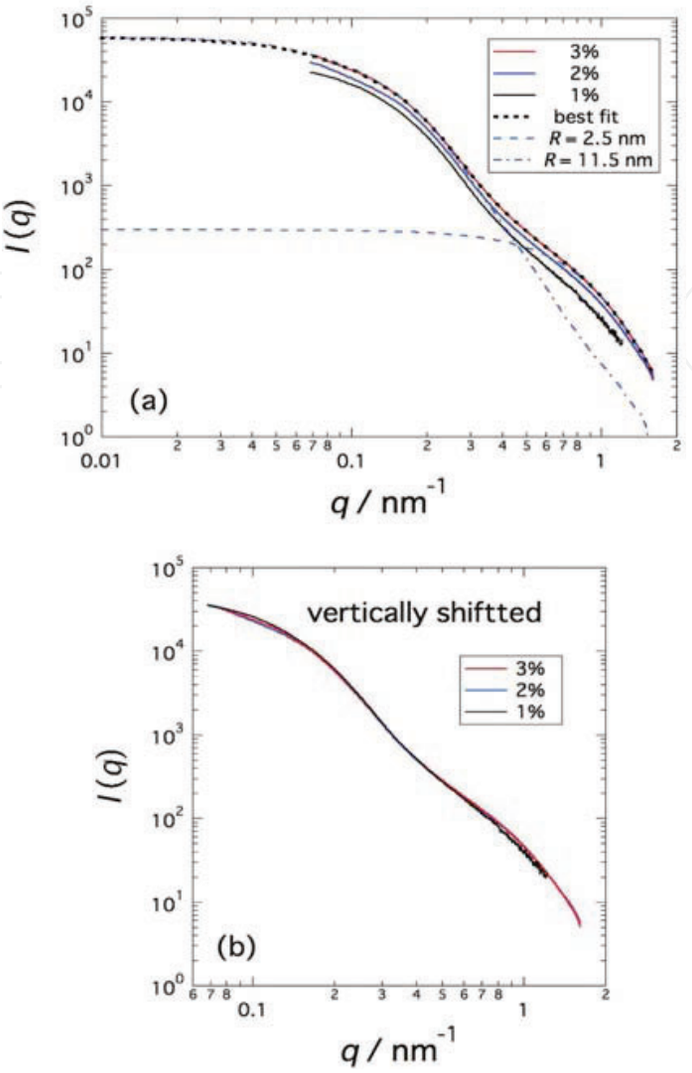

Figure 18. (a) SAXS profiles of 1, 2, and 3% aqueous dispersions of the PPy-Pd nanocomposite particles as a plot of log [$I(q)$] versus log q. The best-fit curve is shown as a dotted black curve on the 1D-SAXS profile for the 3% aqueous solution (most intense and therefore most reliable). (b) Master curve for the SAXS profile obtained by vertically shifting the three 1D-SAXS profiles in (a) (not shifted in q-axis direction) [28].

$$\text{abundance } (vol\%) = n(R)R^3/\Sigma[n(R)R^3] \times 100 \tag{27}$$

Bimodal size distribution was clearly obtained with two peaks at approximately R = 2.5 and 11.5 nm. It is recognized that smaller particles (assuming $n(R)$ with a single peak at approximately R = 2.5 nm) could explain the shape of the SAXS profile in the higher q range (see the broken curve in **Figure 18a**), whereas larger ones (assuming $n(R)$ with a single peak at approximately R = 11.5 nm) characterized the SAXS profile in the lower q range (see the dotted and broken curve). This result does not indicate the real distribution of the PPy-Pd nanocomposite particles themselves, but the additional abundance of tiny Pd nanoparticles existing in the nanocomposite particles. These speculations are confirmed by TEM observations (**Figure 17**), indicating that the average radius was approximately 16 nm with a unimodal distribution and by close examination of the high-resolution TEM image (R = 2.7 nm; **Figure 17**). Thus, it was possible to evaluate not only the size of 'a bunch of grapes' but also the size of all 'grains of grapes in the bunch.'

http://dx.doi.org/10.5772/105981

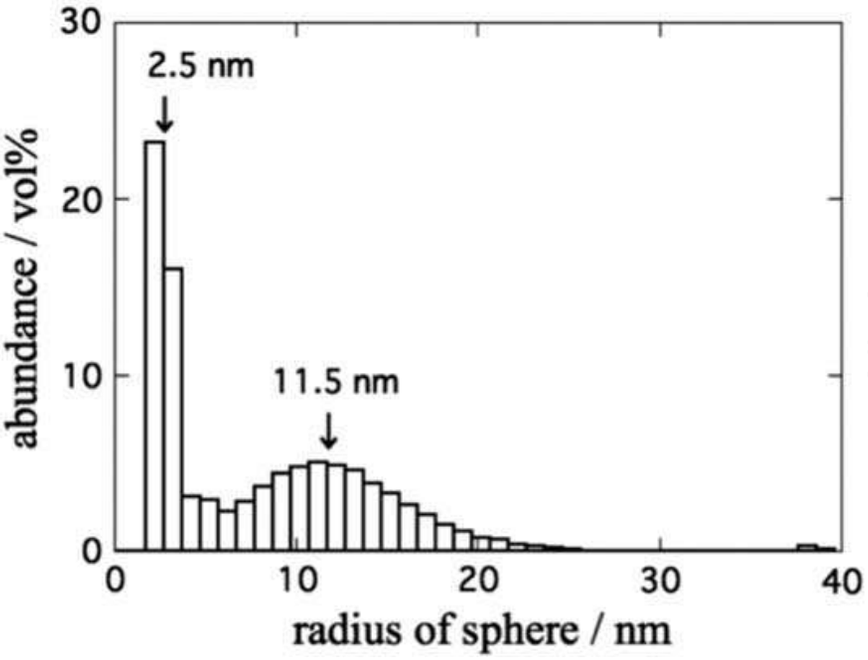

Figure 19. Evaluated particle size distribution based on the result shown in **Figure 18** [28].

Kuroiwa et al. [31, 32] have synthesized novel amphiphilic *N*-isopropylacrylamide (NIPPAm) oligomers with dodecyl groups and carboxyl groups, as shown in **Figure 20a**, by the RAFT polymerization of NIPPAm with *S*-1-dodecyl-*S*′-(*α*,*α*′-dimethyl-*α*″- acetic acid) trithiocarbonate (DTC). It was interestingly found that the DTC-NIPPAm oligomers form network aggregation upon addition of Cu^{2+} ion in an aqueous solution, as revealed by TEM (**Figure 20b** for the dried specimen from an aqueous solution of DTS-NIPPAm35 with Cu^{2+} ions). It seems that the network diameter is somewhat 30 nm or above. There is a possibility to consider that the constitutive unit of the network should be a micelle as schematically illustrated in **Figure 20c**. Since the TEM observation can be only conducted for the dried specimen, the resultant TEM image might be quite different from the real structure in the aqueous media. In order to reveal real structure in the aqueous media, the in situ SAXS measurement was performed at room temperature. Then, the spherical model fitting was applied to the resultant SAXS profile. **Figure 21** shows the SAXS profile with the model form factor. The experimentally obtained SAXS curve (black curve) is available for $q > 0.06$ nm^{-1} and characteristic dent and hump are observed around $q = 0.15$ and 0.50 nm^{-1}, respectively. By assuming the spherical model, the calculated SAXS profile (red curve) can perfectly fit to the experimental one as displayed in **Figure 21**. Thus, evaluated discrete distribution of the radius is shown in **Figure 22**. Here, the main distribution is found around 2–7 nm, implying the cores of the micelles. Because the core contains sulfur atoms, the contrast is considered to be highest and therefore, the core can be the most intense scatterer. This is the reason of observing majority in 2–7 nm in the distribution. This in turn implies that the network aggregation comprises micelles, which can never be detected by TEM. Close examination of the resultant distribution revealed minor abundance around 17 and 21 nm. This agrees well with the least radius of the network aggregation in the TEM observation, as mentioned above. The same distribution is shown in the inset of Figure? with the logarithmic axis for the abundance. Then, it is clear that not only the minor abundance around 17 and 21 nm, but many

minor ones are discernible in the wide range from 17 to 58 nm. As a matter of fact, such big spheres can be occasionally seen in the TEM image (**Figure 20b**). Thus, once again for this kind of complicated aggregation, the method of evaluation of the discrete distribution of size from the SAXS result is approved to be quite effective [33].

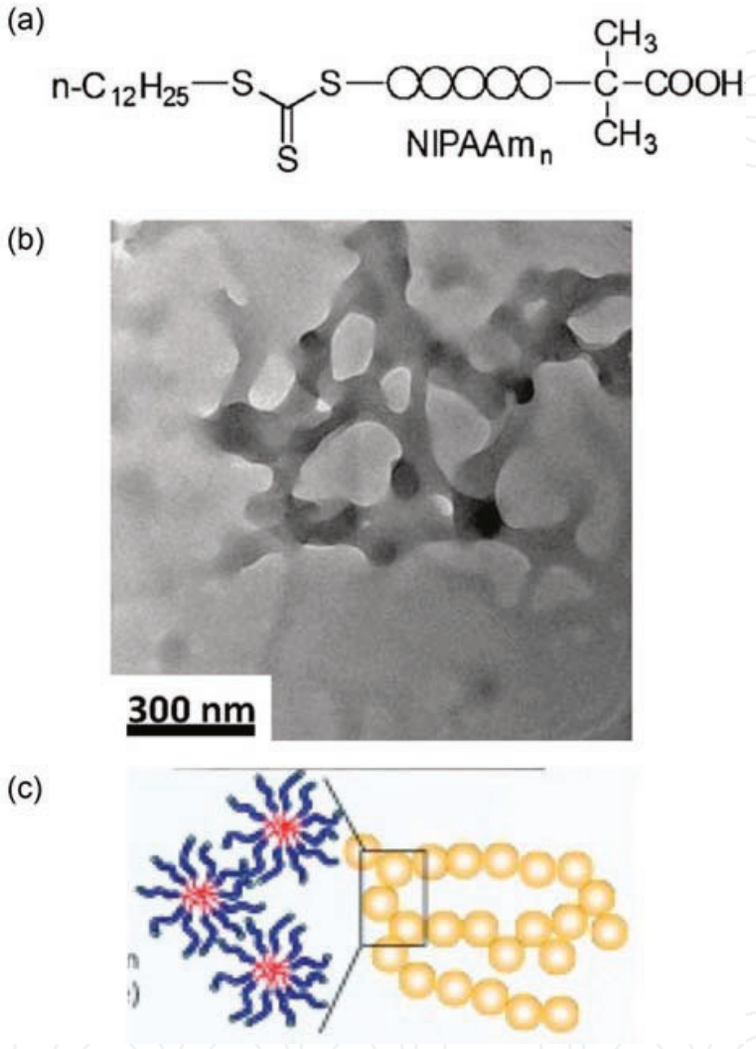

Figure 20. (a) Novel amphiphilic *N*-isopropylacrylamide (NIPPAm) oligomers with dodecyl groups and carboxyl groups. (b) TEM micrograph for the dried specimen from an aqueous solution of DTS-NIPPAm35 with Cu^{2+} ions. (c) Schematic illustration of the micelle network [31, 32].

5. Concluding remarks

In this chapter, we focused on the form factor of a variety of nanostructures (spheres, prolates, core-shell spheres, core-shell cylinders and lamellae). Also getting started with a mono-disperse distribution of the size of the nanostructure, to unimodal distribution with a narrow standard deviation or wide-spreading distribution and finally to the discrete distribution can be evaluated by the computational parameter fitting to the experimentally obtained SAXS profile. In particular, for systems forming complicated aggregations, this methodology is useful. Not only the size

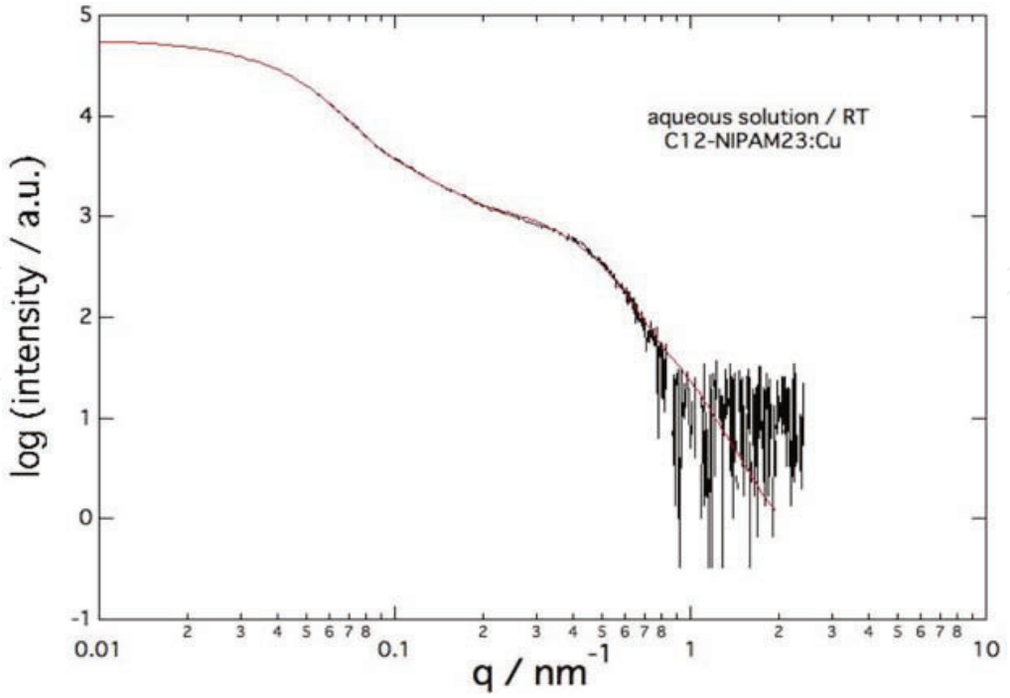

Figure 21. SAXS profile for an aqueous solution of DTS-NIPPAm35 with Cu^{2+} ions with the model form factor. The black curve is the experimentally obtained SAXS profile, and the red curve is the calculated SAXS profile [31, 32].

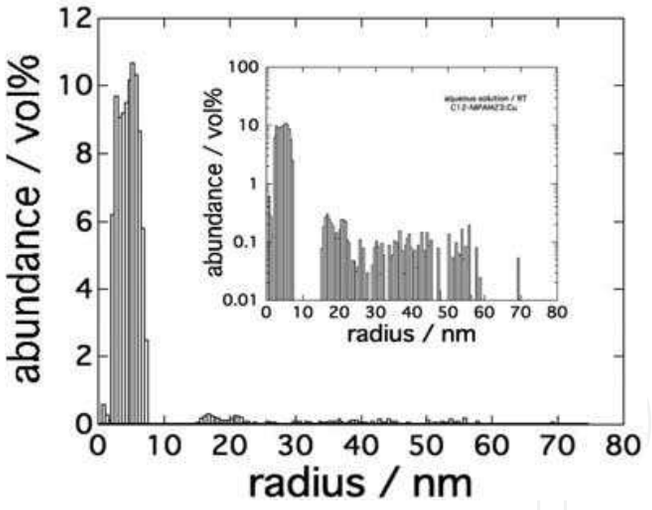

Figure 22. Evaluated size distribution based on the result shown in **Figure 21** [31, 32].

distribution of 'a bunch of grapes' but also the size distribution of all 'grains of grapes in the bunch' can be evaluated according to this methodology. This is very much contrasted to the case of the DLS technique by which only 'a bunch of grapes' is analyzed but 'grains of grapes in the bunch' cannot be. It is because the DLS technique in principle evaluates diffusion constants of particles and all of the grains in the same bunch of grapes diffuse as a whole. Thus, the methodology is important to highlight versatility and diversity in real materials, especially in soft matter,

both in the liquid and in the solid states. At present, however, the shape of the nanostructure is limited in spherical or lamellar. On extending the methodology to the complicated structures such as cylinder, prolate, oblate, or core-shell type, there are tremendous difficulties. For cylinder, prolate, or oblate, difference in the degree of orientation of such particles spoils the methodology such that the size distributions for two principal directions (height and radius for the cylinder case/long axis radius and short axis radius for the prolate and oblate cases) cannot be uniquely evaluated. As for core-shell type particles, the inner and outer radii couple to alter its form factor, so that the size distributions for them cannot be uniquely evaluated either. As a matter of fact, the size distribution is introduced with keeping constant of the ratio of the inner and outer radii for the core-shell spheres [16]. Similarly, for the core-shell cylinders [20], the size distribution in the core radius is incorporated, while the radial shell thickness is assumed to be monodisperse. For more detailed structure analyses, more experimental variations are required to gather information from different kinds of aspects, like the example shown in **Figure 6a** and **b** (parallel and perpendicular to SD). These difficulties should be overcome.

Author details

Shinichi Sakurai

Address all correspondence to: shin@kit.ac.jp

Department of Biobased Materials Science, Kyoto Institute of Technology, Matsugasaki, Sakyo-ku, Kyoto, Japan

References

[1] S. Kobayashi, M. Klaus (Eds.), Encyclopedia of Polymeric Nanomaterials, Springer, New York (2015).

[2] W. H. de Jeu, Basic X-ray Scattering for Soft Matter, Oxford University Press, Oxford, UK (2016).

[3] J. S. Pedersen, Adv. Colloid Interface Sci., 70, 171–210 (1997).

[4] M. Kim, Y. Rho, K. S. Jin, B. Ahn, S. Jung, H. Kim, M. Ree, Biomacromolecules, 12(5), 1629–1640 (2011).

[5] D. Sato, H. Ohtomo, Y. Yamada, T. Hikima, A. Kurobe, K. Fujiwara, M. Ikeguchi, Biochemistry, 55(2), 287–293 (2016).

[6] A. V. Semenyuk, D. I. J. Svergun, Appl. Crystallogr, 24, 537 (1991).

[7] T. Fujisawa, K. Inoue, T. Oka, H. Iwamoto, T. Uruga, T. Kumasaka, Y. Inoko, N. Yagi, M. Yamamoto, T. Ueki, J. Appl. Crystallogr, 33, 797–800 (2000).

[8] U-S. Jeng, C. H. Su, C.-J. Su, K.-F. Liao, W.-T. Chuang, Y.-H. Lai, J.-W. Chang, Y.-J. Chen, Y.-S. Huang, M.-T. Lee, K.-L. Yu, J.-M. Lin, D.-G. Liu, C.-F. Chang, C.-Y. Liu, C.-H. Chang, K. S. Liang, J. Appl. Crystallogr, 43, 110–121 (2010).

[9] T. Sibillano, L. De Caro, D. Altamura, D. Siliqi, M. Ramella, F. Boccafoschi, G. Ciasca, G. Campi, L. Tirinato, E. Di Fabrizio, C. Giannini, Sci. Rep., 4, 6985 (2014). doi:10.1038/srep06985

[10] S. Aida, S. Okamoto, S. Sakurai, J. Masamoto, S. Nomura, Mater. Soc. Res. Int., 7, 234 (2001).

[11] H. Matsuoka, H. Tanaka, T. Hashimoto, N. Ise, Elastic scattering from cubic lattice systems with paracrystalline distortion. Phys. Rev. B, 36, 1754 (1987).

[12] H. Matsuoka, H. Tanaka, T. Hashimoto, N. Ise, Elastic scattering from cubic lattice systems with paracrystalline distortion. II. Phys. Rev. B, 41, 3854 (1990).

[13] T. Kota, K. Imaizumi, S. Sasaki, S. Sakurai, Polymers, 3, 36–50 (2011).

[14] K. Imaizumi, T. Ono, T. Kota, S. Okamoto, S. Sakurai, J. Appl. Crystallogr., 36, 976–981 (2003).

[15] S. Tomita, N. Shimizu, N. Igarashi, H. Takagi, S. Sasaki, S. Sakurai, to be published (2016).

[16] J. Wagner, J. Appl. Crystallogr., 37, 750–756 (2004).

[17] I. Akiba, A. Takechi, M. Sakou, M. Handa, Y. Shinohara, Y. Amemiya et al., Macromolecules, 45, 6150–6157 (2012).

[18] J. S. Pedersen, C. Svaneborg, K. Almdal, I. W. Hamley, R. N. Young, Macromolecules, 36, 416−433 (2003).

[19] Y. Sanada, I. Akiba, K. Sakurai, K. Shiraishi, M. Yokoyama, E. Mylonas et al., J. Am. Chem. Soc., 135, 2574–2582 (2013).

[20] J. B. Matson, C. J. Newcomb, R. Bitton, S. I. Stupp, Soft Matter, 8, 3586–3595 (2012) (and the supporting information).

[21] S. Sakurai, S. Okamoto, T. Kawamura, T. Hashimoto, J. Appl. Crystallogr., 24, 679–684 (1991).

[22] N. D. Tien, T. P. Hoa, M. Mochizuki, K. Saijo, H. Hasegawa, S. Sasaki, S. Sakurai, Polymer, 54, 4653–4659 (2013).

[23] M. Shibayama, T. Hashimoto, Macromolecules, 19(3), 740–749 (1986).

[24] N. D. Tien, T. P. Hoa, G. Kimura, Y. Yamashiro, H. Fujiwara, M. Mochizuki, S. Sasaki, S. Sakurai, J. Phys. Conf. Ser., 272, 012007-1–012007-7 (2011).

[25] N. D. Tien, S. Sasaki, H. Masunaga, N. Shimizu, N. Igarashi, S. Sakurai, Polymer, 55, 2562–2569 (2014).

[26] N.-D. Tien, S. Sasaki, S. Sakurai, Polym. Bull., 73, 399–408 (2016).

[27] J. Scavuzzo, S. Tomita, S. Cheng, H. Liu, M. Gao, J. P. Kennedy, S. Sakurai, S. Z. D. Cheng, L. Jia, Macromolecules, 48, 1077–1086 (2015).

[28] H. Takeoka, N. Fukui, S. Sakurai, Y. Nakamura, S. Fujii, Polymer J., 46, 704–709 (2014).

[29] H. Takeoka, S. Wada, S. Yusa, S. Sakurai, Y. Nakamura, S. Fujii, J. Adhes. Soc. Jpn., 51 (S1) (special issue on WCARP-V), 255–263 (2015).

[30] Y. Chujo, K. Tanaka, Bull. Chem. Soc. Jpn., 88, 633–643 (2015).

[31] K. Kuroiwa, C. Higuma, Y. Shimogawa, H. Hachisako, S. Sakurai, Kobunshi Ronbunshu, 71, 457–466 (2014) (in Japanese).

[32] K. Kuroiwa, Y. Koga, Y. Ishimaru, T. Nakashima, H. Hachisako, S. Sakurai, Polym. J., 48, 729–739 (2016).

[33] K. Kuroiwa, T. Arie, S. Sakurai, S. Hayami, T. J. Deming, J. Mater. Chem. C, 3, 7779–7783 (2015).